




Relativistic Shear Boundary Layer and the Gamma-Ray Emission of GW170817

Jacob Spisak¹, Edison Liang¹, Wen Fu¹, and Markus Boettcher² 

¹Rice University, Houston, TX 77005, USA

²North-West University, Potchefstroom, 2520, South Africa

Received 2020 June 6; revised 2020 August 13; accepted 2020 September 6; published 2020 November 9

Abstract

We present an analysis of the radiation characteristics of kinetic shear boundary layers created by relativistic plasma jets. Using a model of electromagnetic field data based on particle-in-cell simulations of an electron–ion plasma, we solve the motion of individual test electrons and compute their instantaneous radiated power and peak frequency. By analyzing a large number of test electrons in this manner, we find two distinct electron populations present around the shear boundary layer. The most highly radiative electrons execute looping motion due to crossed electric and magnetic fields as they are accelerated along the bulk flow of the jet, and eventually cross the shear boundary interface at steep angles. Electrons that never cross the shear boundary interface radiate much less energy as a group. Summing over all of the highly radiative electrons, we compute the distribution of the total radiated energy as a function of the angle relative to the bulk flow. This result has important potential implications for the observed radiation output of short gamma-ray bursts viewed at large angles from the jet axis, such as the neutron star merger event GW170817/GRB 170817A.

Unified Astronomy Thesaurus concepts: [Plasma astrophysics \(1261\)](#); [Gamma-ray bursts \(629\)](#); [Relativistic jets \(1390\)](#)

1. Introduction

Shear boundary layers (SBLs) are created at the interface of plasma flows with different tangential velocities. They are of interest as a potential source of particle energization (Berezhko 1981; Rieger & Duffy 2006) and radiation (Stawarz & Ostrowski 2002) in a variety of astrophysical contexts, such as blazar and gamma-ray burst (GRB) jets. SBLs may be an important source of the radiation in the spine-sheath model of blazar jets, in which a fast-moving jet spine is surrounded by a slower outer sheath (Stawarz & Ostrowski 2002; Ghisellini et al. 2005, 2010; Boettcher 2007). SBL is also a possible source of the observed radiation of some GRB jets (Meszros 2002; Piran 2005), provided the jet is narrow and the observer is viewing the jet at a large angle from the jet axis. This is the case of the neutron star merger event GW170817/GRB 170817A, which was a highly subluminal short GRB (duration ≤ 2 s, Berger 2014). In the collapsar model (MacFadyen & Woosley 1999) of classical long GRBs (duration > 2 s, Piran 2005), the central newly formed black hole launches an ultrarelativistic plasma jet which must punch through the outer envelope of the progenitor star to become visible. The passage of the jet through circumstellar matter (CSM) likely also creates a dissipative SBL at the jet boundary that would emit enhanced radiation. While most popular models of GRB focus on the radiation emitted by shocks created in the outflow (Meszros 2002; Piran 2005), SBL emission may become important in those GRBs, where a large observer viewing angle from the jet axis favors the visibility of the SBL over the frontal shocks (see Section 5).

Numerous recent studies have investigated the formation and structure of collisionless SBLs via particle-in-cell (PIC; Birdsall & Langdon 1991) simulations (Alves et al. 2012, 2014; Grismayer et al. 2013; Liang et al. 2013, 2017, 2018; Nishikawa et al. 2014, 2016). Unlike SBL in the MHD regime (Zhang et al. 2009), these kinetic simulations show that initially unmagnetized neutral shear flows generate strong electromagnetic (EM) fields via collisionless plasma instabilities, such as the electron kinetic

Kelvin–Helmholtz instability (EKKHI; Gruzinov 2008; Alves et al. 2012, 2014; Grismayer et al. 2013), Weibel instability (1959), and the electron counter current instability (ECCI, Liang et al. 2013, 2017, 2018). The radiation properties of the kinetic SBL, however, have not been thoroughly investigated. In a recent paper, Liang et al. (2018) found that the highest energy electrons energized by the SBL are beamed into angles much narrower than $1/\Gamma$ (Γ = bulk Lorentz factor in the laboratory frame or central engine frame). Such narrow beaming may help solve certain issues related to blazar spectra and time variability (Boettcher 2007; Liang et al. 2018). However, the radiation pattern of these narrow electron beams remain to be calculated from first principles.

The goal of this paper is to provide a more accurate and detailed characterization of the radiation emitted by the electrons in the PIC simulation of SBL. In particular, we will analyze individual electron trajectories to determine the mechanisms that generate the most radiation, as well as the angular distribution and peak frequency of this radiation. This will facilitate the comparison of the theoretical predictions of SBL radiation with observational data from blazars and GRBs. Since high-resolution continuous electron trajectories cannot be directly extracted from PIC simulations due to the finite time steps and high-frequency numerical noise inherent in PIC simulations (Birdsall & Langdon 1991; Hededal 2005; Hededal & Norlund 2005; Sironi & Spitkovsky 2009; Nishikawa et al. 2014), here we adopt a different approach to model radiation by solving for continuous test electron trajectories using simplified model electromagnetic fields derived from the PIC simulation. This allows us to obtain more reliable momentum and acceleration histories based on a continuous electron trajectory, from which radiation output can be meaningfully calculated.

This paper is structured as follows. Section 2 provides an overview of the PIC simulation used in our analysis. Section 3 describes the approximations used to solve for the test electron trajectories. In Section 4 we present the results for the simulated trajectories for a large number of representative test

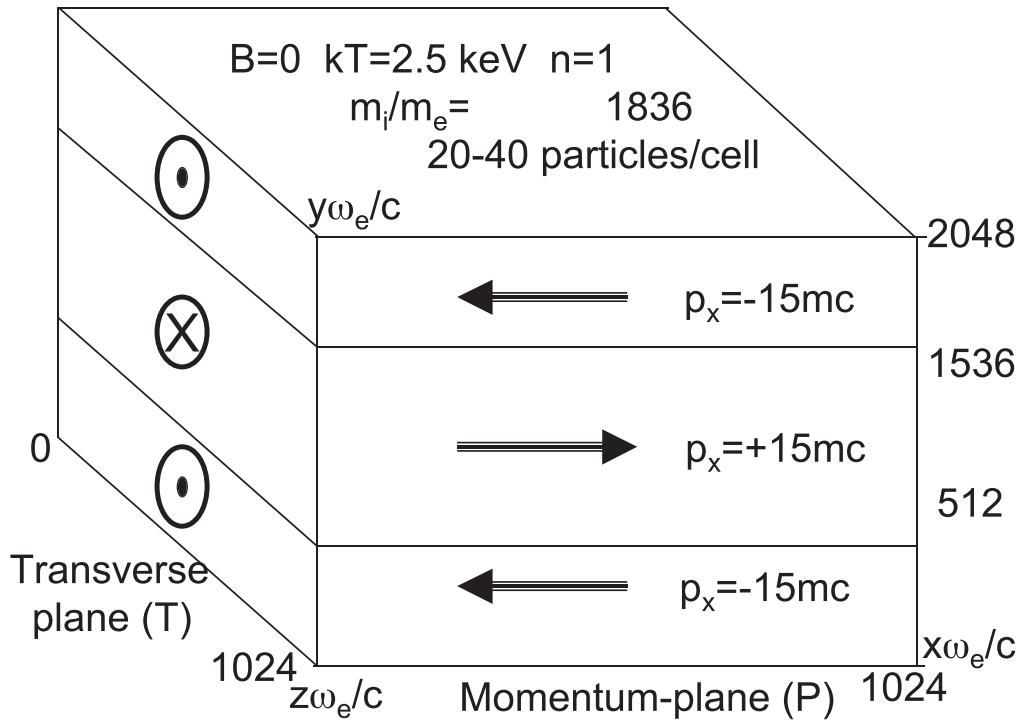


Figure 1. Setup for PIC simulations of shear flows in the center of momentum frame (adapted from Liang et al. 2013). The arrows indicate the direction of the initial bulk flow velocity. Due to the periodic boundary conditions, there are two shear boundaries located at $y\omega_e/c = 512$ and $y\omega_e/c = 1536$. For the radiation calculation of this paper we use the electromagnetic field profiles of a 2D PIC run in the x - y plane with $m_i/m_e = 1836$, whose main results have been validated with both 2D simulations in the y - z plane and 3D simulations.

electrons and their radiation characteristics. In Section 5 we discuss the relevance of our results to the radiation output of the short gamma-ray burst associated with the neutron star merger event GW170817. Conclusions and discussions are provided in Section 6.

2. Particle-in-cell Simulation of SBL

The particle-in-cell (PIC; Birdsall & Langdon 1991) simulation is a standard method used to simulate the kinetic evolution of collisionless plasmas, in which individual coulomb collisions can be ignored compared to collective plasma processes (Krall & Trivelpiece 1973; Boyd & Sanderson 2003). The basic element of a PIC simulation is a superparticle, which represents billions to trillions of real electrons or ions. The motion of the superparticles allows charge and current densities to be computed at grid points, which in turn are used to solve for the electric and magnetic fields from the Maxwell equations. A single time step consists of one full cycle of charge, current, and field calculations. By evolving individual superparticles in their collective mean fields, PIC simulations are able to model collective kinetic processes accurately. This makes them ideal tools for modeling highly collisionless relativistic flows. In this paper, we will use data from a 2D PIC simulation of an electron-proton shear flow for which the main results have already been published in Liang et al. (2013). The PIC simulation setup for the shear flow is shown in Figure 1.

This 2D simulation was run using the 2D ZOHAR code (Birdsall & Langdon 1991; Langdon & Lasinski 1976) and later validated with the 3D EPOCH code (Brady et al. 2012). The simulation consists of an initially unmagnetized electron-proton plasma flowing through the center of the simulation

box, surrounded on both sides by identical but oppositely directed plasma flows. The plasma has initial bulk velocity in the x direction, with a Lorentz factor of $p_o = 15$ in the center-of-momentum (CM) frame, corresponding to a Lorentz factor of $\Gamma = 451$ for the jet spine in the observer or laboratory frame (LF = rest frame of the central engine). This Γ value is typical of known GRBs (Piran 2005; Meszoros 2002). The simulation box is divided into 1024×2048 cells, with periodic boundary conditions in both x and y . The cell size is set equal to the electron skin depth c/ω_e , and the time step is set equal to $\Delta t = 0.1/\omega_e$, where ω_e is the electron plasma frequency (Boyd & Sanderson 2003). Each cell contains 20 superparticles, and the plasma has an initial temperature of 2.5 keV for both species. The plasma is initially unmagnetized and spatially uniform, except for the drift velocity reversals at $y = 512$ and 1536 (Figure 1; Liang et al. 2013).

As the simulation evolves, instabilities due to electron counter currents on opposite sides of the SBL create double slabs of d.c. magnetic and electric fields (Figure 2), which eventually saturate at approximately 8% of the total system energy (Figure 3; Liang et al. 2013). Bulk flow kinetic energy is converted to high-energy electrons accelerated by self-generated EM fields, which should lead to prolific synchrotron-like radiation (Rybicki & Lightman 1979). The dominant d.c. fields are E_y and B_z , which form just outside the shear flow interface and are uniform in the x direction to first order (Figures 2(a), (b)). A small inductive E_x field is also created by the time-variation of B_z (Figure 2(c)). To confirm the validity of the 2D simulations in the x - y plane, additional simulations were run with the same setup both in the 2D y - z plane and in 3D (Liang et al. 2013). Instabilities in the y - z plane grow very slowly compared to those in the x - y plane, indicating that the

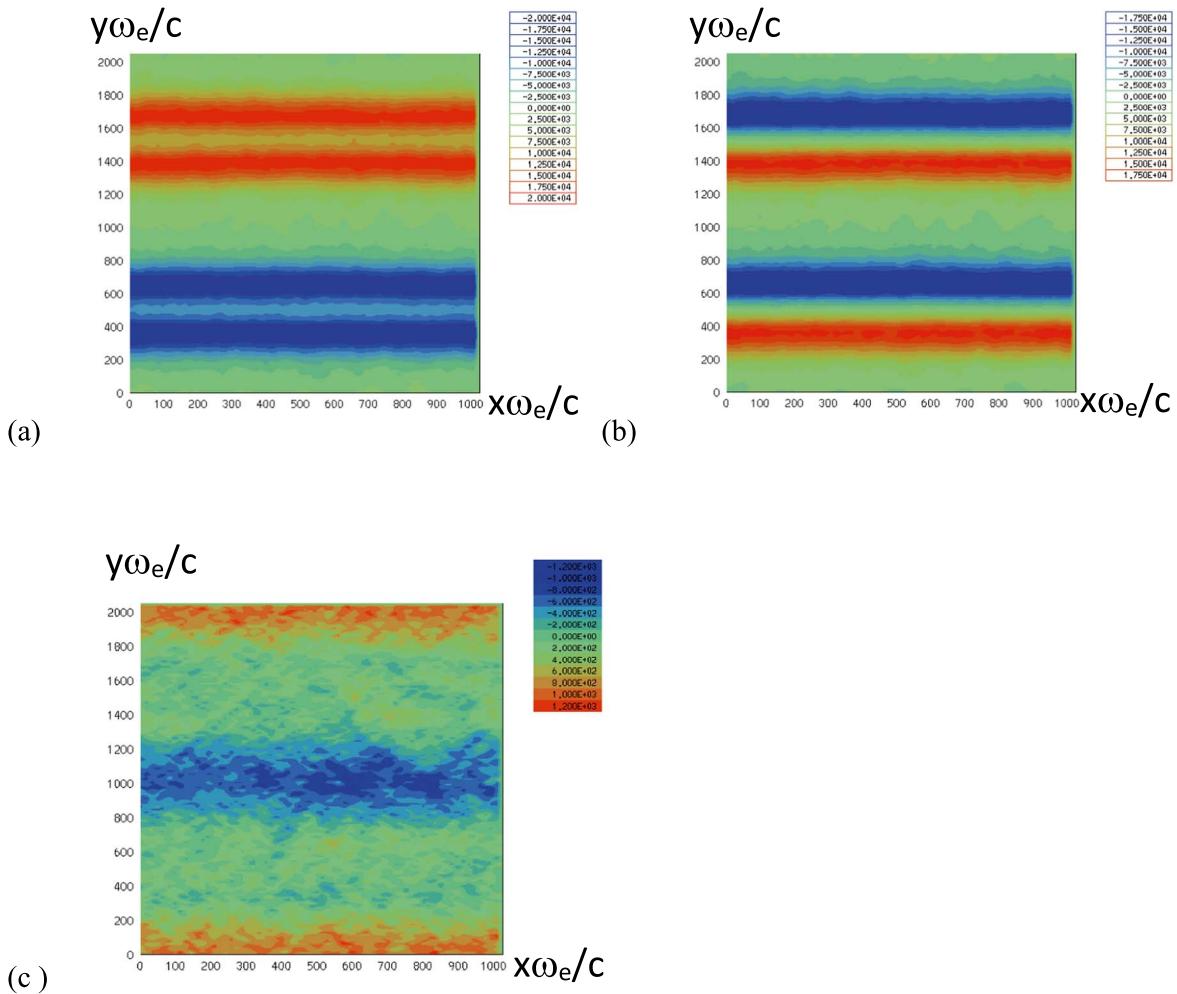


Figure 2. Sample electromagnetic field profiles in the x - y plane of Figure 1 at $\omega_c = 8000$: (a) B_z , (b) E_y , and (c) E_x . Field amplitudes and color scales are not normalized. Contour plots are averaged over eight cells to smooth out the high-frequency noise.

latter contains most of the field growth leading to the final SBL structure. The 3D simulation comparison was run using the PIC code EPOCH (Brady et al. 2012). While it was limited to a box size of only $128 \times 2048 \times 64$ due to computational constraints, it exhibited shear boundary layer properties similar to the 2D x - y simulation (Liang et al. 2013). In addition, we have studied shear flows with a broad transition zone and gentle velocity gradients and found that the basic properties of the SBL, such as the d.c. electromagnetic field profiles of Figure 2 and accelerated electron distributions, remain similar to those reported in Liang et al. (2013). We emphasize that the unmagnetized, pure electron-ion plasma assumed in this work represents only the first step in the broader study of realistic shear flows. Generalizations of the above PIC simulation to include mixed compositions, preexisting magnetic fields, density jumps, and other complexities will be discussed in Section 6.

3. Radiation Modeling

The next step is to compute the radiation output from SBLs emitted by an ensemble of test electrons (Heddal & Norlund 2005; Sironi & Spitkovsky 2009; Nishikawa et al. 2014) using a simplified model of EM fields based on the PIC simulation. This involves computing individual electron

trajectories, radiation power output, and peak radiation frequency, all of which require continuous position, momentum, and acceleration information. These quantities cannot be computed directly from the PIC simulation itself, because the raw PIC data are too noisy in both time and space to be useful for meaningful radiation calculations. In the past, we have attempted to compute the radiation using tracer particles imbedded in the PIC simulation. However, the output was too noisy and it was difficult to extract useful quantitative results. Our new approach to this problem is to step outside the confines of the PIC simulation to solve for the test electron trajectories. Using a model of the electromagnetic fields derived from the PIC simulation plus a set of simplifying assumptions, we solve the Lorentz force equations for individual test electrons and use their continuous trajectories to compute the radiation quantities. Given a sufficiently large and representative sample of initial electron conditions taken from the PIC simulation, this approach allows us to characterize the collective radiation emitted by an ensemble of test electrons.

We solve for the position and momentum time histories of each test electron using the following set of coupled ordinary differential equations, working in units where $e = m_e = c = 1$. (We ignore electron motion in the z -direction since $E_z = 0$ in 2D PIC simulations, and our 3D PIC simulations also confirm

that $p_z \ll p_x, p_y$).

$$dx/dt = p_x/\gamma \quad (1)$$

$$dy/dt = p_y/\gamma \quad (2)$$

$$dp_x/dt = -E_x - p_y^* B_z/\gamma \quad (3)$$

$$dp_y/dt = -E_y + p_x^* B_z/\gamma \quad (4)$$

$$\gamma = (1 + p_x^2 + p_y^2)^{1/2}. \quad (5)$$

In order to construct the field models of E_x , E_y , and B_z to accelerate the test electrons, we use the field data from the PIC simulation of Liang et al. (2013) at $t\omega_e = 5000$ and 8000 . In this particular case, the fields evolve very little from $t\omega_e = 4000$ to $t\omega_e = 10,000$, when almost all electron radiation is emitted. We have carefully compared the fields at $t\omega_e = 5000$ and 8000 and found very little difference in their B_z and E_y profiles. More importantly, we have examined a large number of test electron trajectories computed using the fields at $t\omega_e = 5000$ and $t\omega_e = 8000$, and found no systematic differences. We have further spot-checked electron trajectories computed using fields at other times between $t\omega_e = 4000$ and $t\omega_e = 10,000$, and also found no systematic difference from the trajectories calculated using the fields at these two specific times. Hence we are confident that from $t\omega_e = 4000$ to $t\omega_e = 10,000$, the global ensemble of test electron trajectories and their radiation histories can be reasonably represented by using the static field models based on the snapshots at $t\omega_e = 5000$ and $t\omega_e = 8000$. Any time evolution of the d.c. fields during this period is very slow and small, with negligible effects on the electron trajectories. The PIC simulation outputs a 2D array of field data evaluated at the nodes of the simulation grid. Using Mathematica’s built-in Hermite interpolation method, these PIC-simulated field data arrays are used to create smoothed continuous functions of y . To focus on a single shear boundary layer, we use only the top half of the PIC simulation box shown in Figure 1 and shift the y coordinate by 1024 units so that the upper shear interface is relocated to $y = 512$. To simplify the calculations, the field variables are averaged over all x (Figure 2), and averaged over four cells in the y -direction to get rid of high-frequency numerical noise. From previous scaling studies we found that the small variations of the d.c. fields along x depend on the box size. Such small variations are likely numerical rather than physical, caused by the periodic boundary condition. As a first approximation we therefore decide to ignore any x -dependence, and leave such inhomogeneity effects to future scaling studies. In the y -direction, we extrapolate the fields to $y = +/\infty$ beyond the half simulation box by letting them decay as $1/|y|$ for $y \gg 1024$ and $y \ll 0$. This way the test electrons do not get artificially recycled repeatedly across the SBL, as they were in the periodic PIC boxes. The smoothed field profiles for $t\omega_e = 8000$ as functions of y are shown in Figure 4.

We solve Equations (1)–(5) numerically using Mathematica’s built-in Implicit Runge–Kutta method with Gauss–Legendre coefficients and Newton’s method as the nonlinear solver. We adopt the default values of all other parameters of the ODE solver. We note that Equations (1)–(5) ignore radiation damping terms (Landau & Lifshitz 1962; Rybicki & Lightman 1979). A detailed analysis of many electrons described later in the paper yielded a maximum radiative energy loss that is several orders of magnitude less than the energized electron kinetic energy. Hence we conclude that

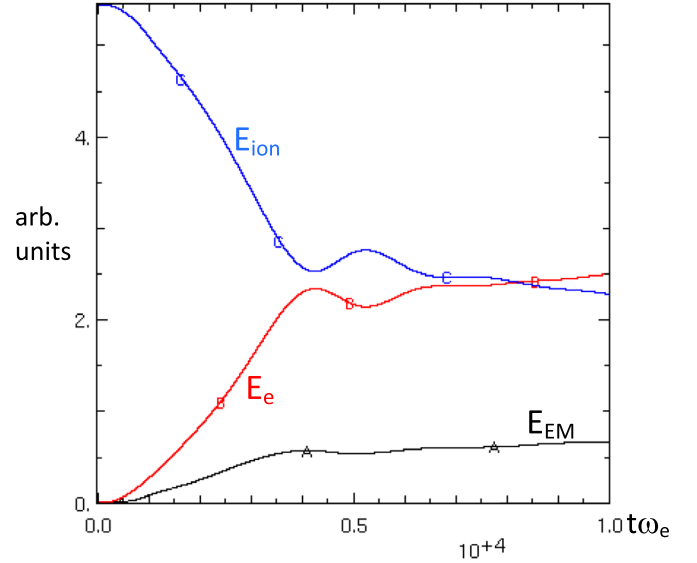


Figure 3. Time histories of the energy components (arbitrary units) for the shear flow of Figure 1. Curve A: EM fields (black), Curve B: electrons (red), Curve C: ions (blue).

radiative energy loss and radiation damping are negligible for the duration of our calculations and can be safely ignored.

4. Results

We computed the electron trajectories using a representative sample of initial conditions taken from the PIC simulation results. Without loss of generality, only “spine” electron trajectories starting from initial locations below $y = 512$ of Figure 4 are presented in this paper, since those initially located above $y = 512$ (“sheath” electrons) execute identical motions moving in the opposite direction.

Representative electron trajectories are shown in Figure 5 for a variety of initial conditions. Electrons with large initial p_{x0} and y_0 close to the shear interface ($y = 512$) tend to swiftly cross the interface without looping motion and shoot off to $y = +\infty$ (upper left panel). These electrons radiate the most total energy. In the opposite limit, electrons with small y_0 swiftly move away from the interface to $y = -\infty$ (upper right panel). These electrons radiate the least total energy. In all other cases, the electron executes multiple loops until it either crosses the shear interface, sometimes multiple times, before finally shooting off to $y = +$ or $y = -\infty$ without ever crossing $y = 512$ (see the second right panel of Figure 5). In all interface-crossing trajectories, the radiative power peaks when the electron crosses the interface the last time before shooting off to $y = +/\infty$. The looping behavior can be explained by recalling the analytic solution to the motion of an electron in crossed electric and magnetic fields. For an electron injected with momentum in the $+x$ direction, the force contributions from B_z and E_y are parallel, opposite, and nearly equal in magnitude, with the former pointing in $+y$ and the latter in $-y$. For simplicity, E_x is ignored to first order since its magnitude is much less than B_z and E_y , and it contributes no force along y . In the case of spatially constant E_y and B_z , the solution is simply a circular motion in a reference frame with drift velocity $= |E_y/B_z|$ in the $+x$ direction (Landau & Lifshitz 1962). Transforming back to the rest frame of the fields then yields stretched loops moving

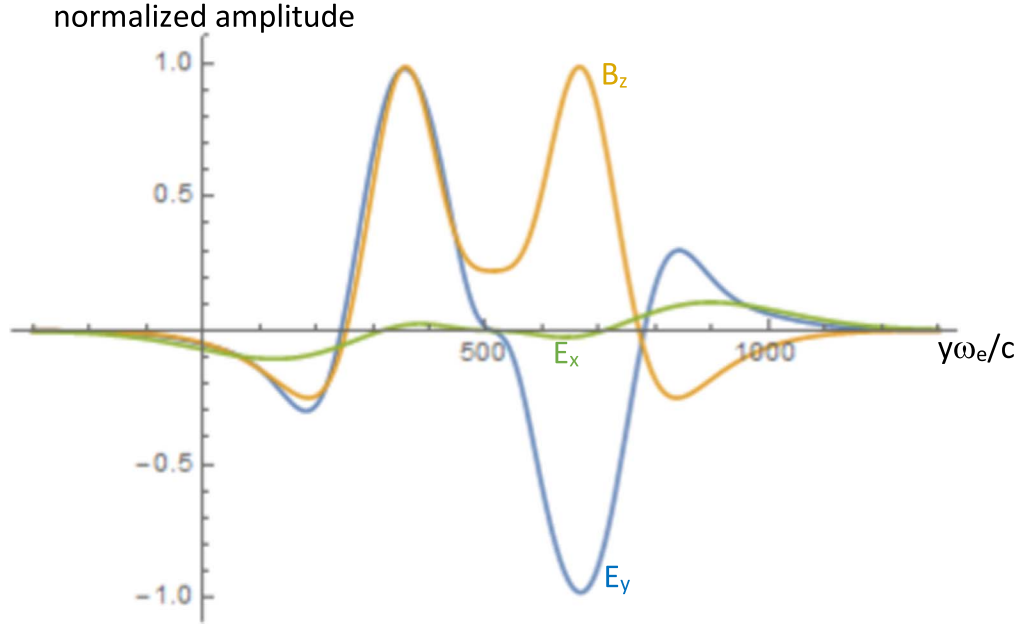


Figure 4. Model profiles for E_x (green), E_y (blue), and B_z (orange) derived from the upper half of the PIC box of Figure 2, averaged along x and plotted as functions of y . Field amplitudes have been averaged over four y -cells and extrapolated beyond the original upper half of the PIC box to $y = \pm\infty$. In this and all subsequent figures, the upper shear interface has been relocated to $y = 512$ after we have shifted the y coordinate by 1024 units.

in the $+x$ direction. While this analogy is not perfect because the SBL fields are not spatially constant, it agrees qualitatively with the looping behavior seen in Figures 5. These loops drift toward $y = 512$ as the electron reaches higher and higher energies. As the electron approaches $y = 512$, B_z rapidly dominates over E_y (see Figure 4), causing the electron to cross the shear interface. At the last crossing, the electron typically gains enough energy so that $\gamma > 10^4$. This high γ plus the strong transverse force experienced by the crossing are the main causes of the spike in the radiative power (Rybicki & Lightman 1979).

The second type of electron trajectory, seen in the top two panels of the right column, corresponds to electrons that never cross the shear interface. This behavior is typical of electrons with an initial $y_0 < 150$. The electron may undergo zero, one, or more loops, while moving away from the shear interface and finally shoots off to $y = -\infty$. These electrons radiate little radiation due to the small forces they encounter or their low γ or both.

Using the solution of Equations (1)–(5), the instantaneous radiative power of an electron can be computed using the relativistic dipole formula (Rybicki & Lightman 1979):

$$P_{\text{rad}} = (2/3)[(dp_x/dt)^2 p_x^2 + (dp_y/dt)^2 p_y^2 + \gamma_*^2((dp_x/dt)^2 p_y^2 + (dp_y/dt)^2 p_x^2)] / (p_x^2 + p_y^2) - (4/3)(dp_x/dt)(dp_y/dt)p_x p_y. \quad (6)$$

We can also compute the peak radiation frequency (also called the “critical frequency” in classical synchrotron radiation with constant B field; Rybicki & Lightman 1979). Because our electrons are highly relativistic, their radiation is beamed within a cone of half angle $\delta\theta \sim 1/\gamma$ around the electron’s instantaneous velocity vector. Since typical angular displacements along the trajectories are much larger than $1/\gamma$, following Landau & Lifshitz (1962), the instantaneous peak radiation frequency can be approximated as (modulo a

numerical factor of order unity):

$$\omega_{\text{rad}} \sim \gamma_* |(dp_x/dt)p_y - (dp_y/dt)p_x|. \quad (7)$$

Equation (7) reduces to the usual critical frequency of synchrotron radiation in a constant B field if we set $E_x = 0 = E_y$ in Equations (3) and (4). The time histories of P_{rad} and ω_{rad} in the CM frame are plotted in Figure 6 for two examples: (a) a highly radiative electron, and (b) a low radiation electron, together with their y positions as functions of time for reference. Figure 6(a) shows the radiation history of an electron with $y_0 = 300$. Its radiative power steadily increases during the extended looping motion. Soon after the electron crosses the shear interface at $y = 512$, the radiative power spikes by a factor of $\sim 10^2$ due to a sharp rise in γ and transverse force. During this brief radiated power surge, up to 80% of the total radiated energy is emitted *at large angles from the flow direction*. Such behavior is common among the highly radiative electrons. On the other hand, the electron starting at $y_0 = 100$, shown in Figure 6(b), radiates much less energy than its counterpart starting at $y_0 = 300$. These results indicate that crossing the shear interface at a large angle from the flow direction is characteristic of a highly radiative electron. Figure 6 shows that the peak radiation frequency ω_{rad} (see Equation (7)) follows a similar pattern as P_{rad} . But the spike in ω_{rad} due to crossing the shear interface at a large angle is only a factor of ~ 10 . When we factor in the transverse Doppler effect after ω_{rad} is Lorentz transformed from the CM frame to the laboratory frame (LF = central engine rest frame, Rybicki & Lightman 1979), the observed ω_{rad} in the LF actually varies little during boundary crossing. For the same reason, the large P_{rad} spike in Figure 6(a) caused by the interface crossing makes only a moderate contribution to the received radiation energy in the LF because of the transverse Doppler effect (see Section 5).

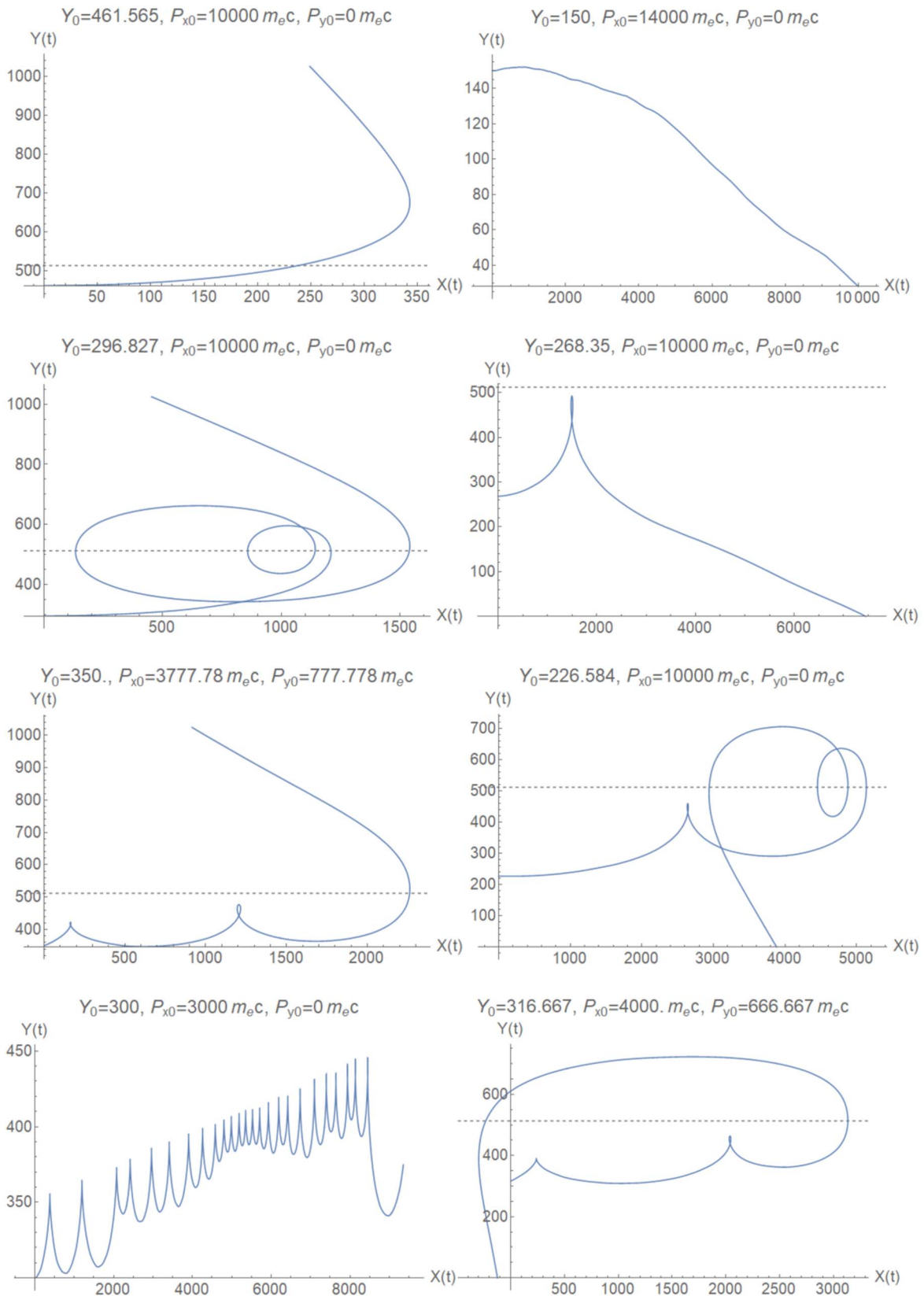


Figure 5. Sample electron trajectories in the x - y plane solved using the field models of Figure 4, showing the diversity of their shapes. The dashed line at $y = 512$ denotes the upper shear interface of Figure 2. Initial conditions are listed at the top of each figure. All trajectories in the left column eventually terminate at $y = +$ infinity, while those in the right column eventually terminate at $y = -$ infinity. Top row highlights trajectories without looping motion, while all other trajectories execute looping motion, with some trajectories crossing the shear interface multiple times. x and y coordinates are expressed in units of c/ω_e .

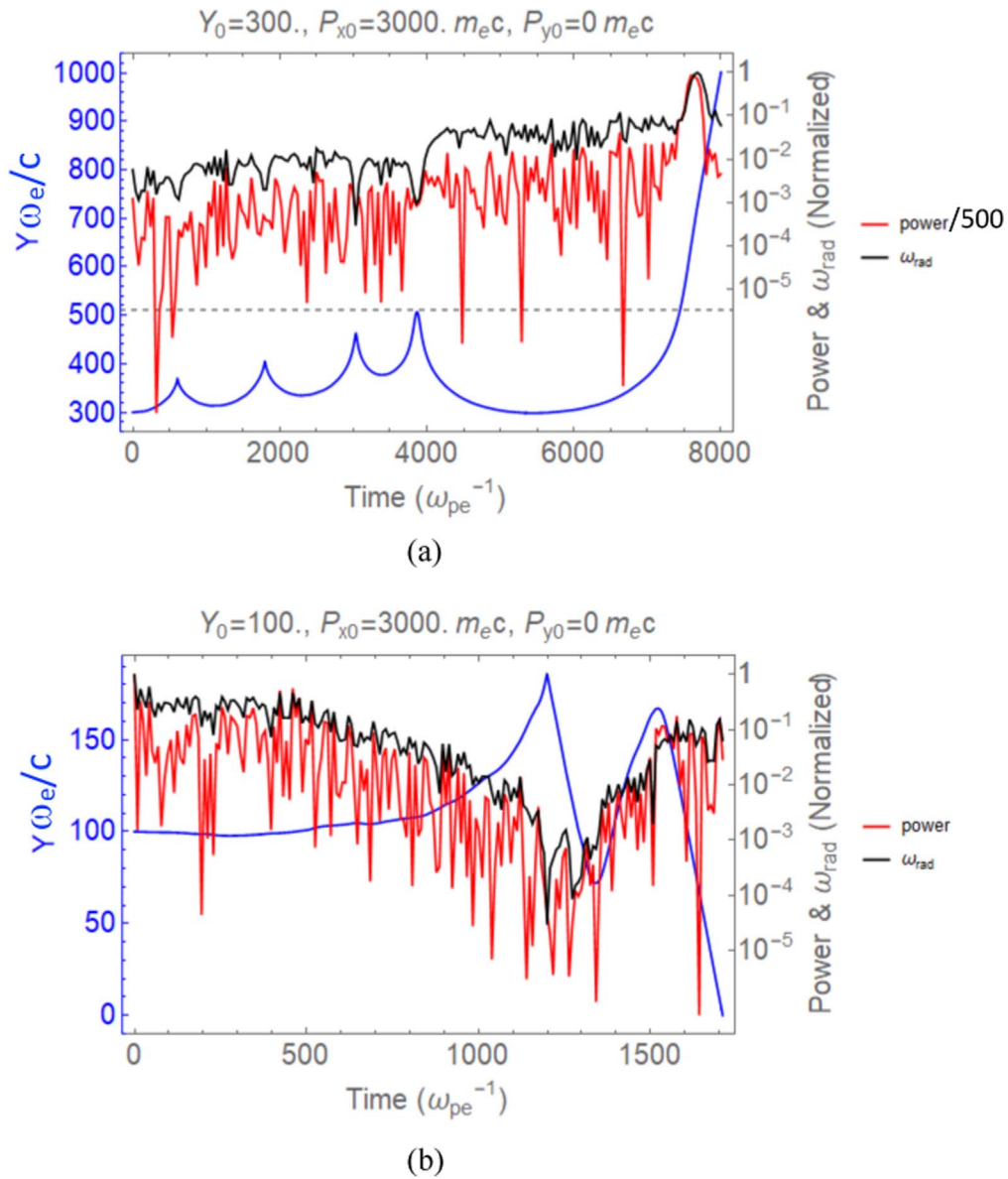


Figure 6. Time histories of radiative power P_{rad} (red), critical frequency ω_{rad} (black), and y position (blue) for two electrons: (a) a highly radiative electron that crosses the shear interface at $y = 512$, (b) a low radiation electron that never crosses the interface. The right vertical scales of the top panel are normalized relative to those of the bottom panel. But the scale of ω_{rad} is unrelated to the scale of P_{rad} . The maximum P_{rad} of the electron in (a) is over 1000 times higher than that of the electron in (b).

Using the Stampede2 supercomputer at UT Austin, we have computed several thousand electron trajectories across a broad range of uniformly sampled initial conditions in y_0 , p_{x0} , and p_{y0} , based on the electron distributions of the PIC simulation (Liang et al. 2013). Roughly two-thirds of the test electron trajectories of our ensemble were computed using the static field model at $t\omega_c = 5000$, and one-third of the trajectories were computed using the static field model at $t\omega_c = 8000$ (Figure 4). As we stated in Section 3, there are no systematic differences between the two sets of electron trajectories. Hence we are justified in combining the two sets. The relative number of electron trajectories emitting different total energies is shown as a histogram in Figure 7. This histogram shows two distinct electron populations, one with high radiation energy and one with low radiation energy, corresponding to the two types of trajectories shown in Figure 6. The high radiation population consists of electrons similar to those shown in

Figures 6(a), while the low radiation population consists of electrons similar to those in Figures 6(b). The high radiation population, starting at around energy $\sim 2 \times 10^{12}$ (arb. units), emits 95% of the total energy radiated by all test electrons in the CM frame.

Aggregating the above results, we can compute the angular distribution of total radiation from all test electrons. For this analysis we include only electrons from the high radiation population. Since the emitted radiation from a relativistic particle is beamed into a narrow cone of half angle $\sim 1/\gamma$ around the instantaneous velocity vector (Rybicki & Lightman 1979) and $\gamma \gg 1$, to first order we can approximate the instantaneous radiation as a pencil beam pointed in the direction of the electron velocity. Defining θ as the angle from the x -axis of the PIC box (Figure 1), we divide θ into 1° bins and calculate the total energy radiated into each angular bin by time-integrating P_{rad} along each trajectory. Summing these

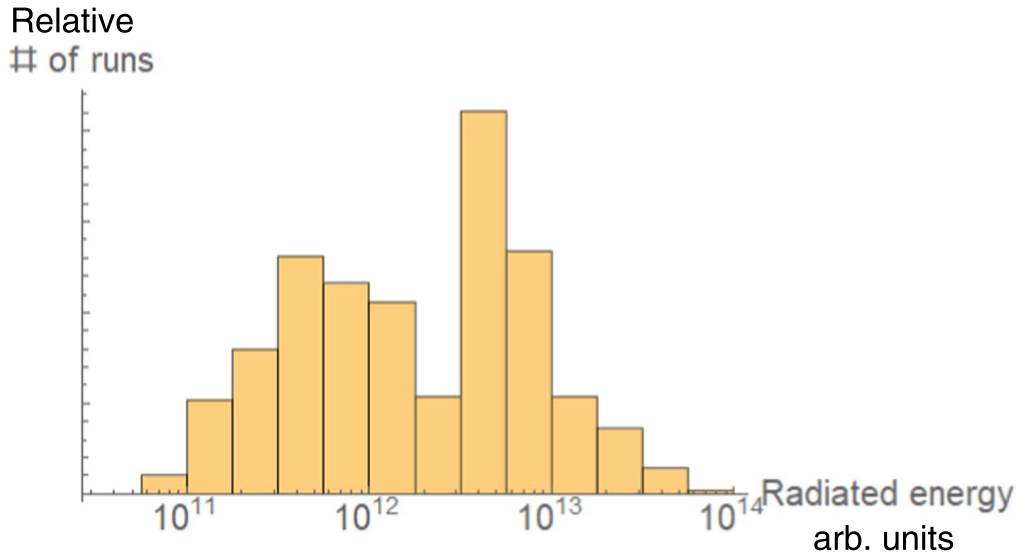


Figure 7. Relative histogram of total radiated energy for the ensemble of test electron trajectories. The right peak corresponds to the high radiation population and the left peak to the low radiation population. Markers on the vertical axis denote the relative number of runs in each energy bin.

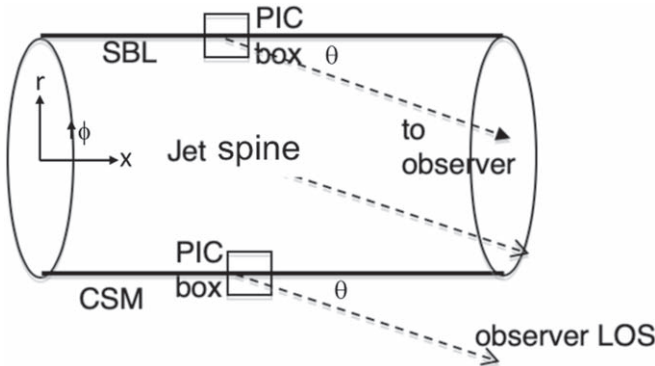


Figure 8. Schematic diagram illustrating the geometry used in a ray-tracing calculation of the global radiation angular pattern of a cylindrical jet shear boundary which is uniform in ϕ and x . Each 2D PIC box represents a small, thin, radial r - x slice of the cylindrical shear boundary. The assumed azimuthal and axial symmetries of the shear boundary allow us to add up the radiation output of all identical PIC boxes in the ϕ -and- x directions. The globally integrated radiation pattern depends only on the angle θ between the observer and the x -axis. Because the radiation of each PIC box is computed in the center of the momentum frame, the global radiation output will need to be Lorentz boosted to the laboratory or observer frame to compare with observations. Here CSM denotes circumstellar matter that is stationary in the laboratory frame.

distributions over all test electrons yields the global radiation angular distribution of the 2D SBL, assuming that our test electron ensemble is representative of the entire electron population. Next we assume that each 2D PIC box corresponds to a small thin 2D radial slice of a global cylindrical jet boundary (Figure 8) uniform in ϕ and in x . Utilizing the ϕ -symmetry, we can obtain the ϕ -integrated total energy emitted by the cylindrical boundary layer per unit solid angle $dE_{\text{rad}}/d\Omega$ by dividing by $d\Omega = 2\pi\sin\theta d\theta$. This global radiation angular distribution of a cylindrical SBL in the CM frame is shown in Figure 9. The sharp spike around $\theta = 0^\circ$ indicates that the highest intensities will be observed along the x -axis (= the jet axis) of Figure 8. This is despite the fact that for the highly radiative electrons such as that in Figure 6(a), most of the energy is radiated at large θ as the electron crosses the shear interface. Two effects combine to moderate their contribution in Figure 9, which can be seen as a broad bump lying between

100° and 150° . The first is that the boundary-crossing velocity angle varies widely among all electrons, diluting the energy deposited into any particular angular bin. The second is that for a given energy deposited into an angular bin nearly perpendicular to the jet axis, it is spread over a large solid angle in the sky. In contrast, energy beamed into the same 1° bin along the jet axis will be emitted into a much smaller solid angle. Hence the radiation emitted per unit solid angle $dE_{\text{rad}}/d\Omega$ still peaks along the jet axis. This “forward beaming” comes from the cumulative radiation emitted from all sections of the electron trajectory parallel to the x -axis. We note that the secondary peak near 180° is emitted by those electrons reaccelerated in the opposite direction after crossing the shear boundary. We point out that Figure 9 accounts for only the spine electrons. A similar figure with left and right reversed accounts for the sheath electrons.

5. Application to Radiation from GW170817/GRB 170817A

To connect the above results to astrophysical observations, we must first Lorentz boost $dE_{\text{rad}}/d\Omega$ from the CM frame of the PIC box to the observer or laboratory frame (LF = rest frame of the central engine in which the jet spine moves at $\Gamma = 451$ and the sheath is at rest). The resultant radiation angular distribution $dE'_{\text{rad}}/d\Omega'$ versus θ' in the LF is plotted in Figure 10. Figure 10 includes contributions by both the spine and sheath electrons, but the spine contribution completely dominates due to Lorentz boosting to the LF. We see that the forward radiation is now greatly enhanced while the backward radiation is greatly suppressed by Lorentz boosting to the LF, and the broad bumps emitted by electrons crossing the shear boundary at large angles are now reduced to small “knees” at $\sim 2^\circ$ - 5° . However, these “knees” \sim at 2° - 5° are a tell-tale signature of SBL emission. In contrast to the SBL emission angular pattern of Figure 10, the emission from a relativistic planar shock normal to the jet axis, when viewed at angles $\theta \gg \Gamma^{-1}$, falls off as $\sim(\theta\Gamma)^{-8}$ (Rybicki & Lightman 1979), which is much steeper than Figure 10.

We next discuss the potential relevance of Figure 10 to gamma-ray bursts viewed at large angles from the jet axis, such as the case of GW170817/GRB 170817A. We emphasize that

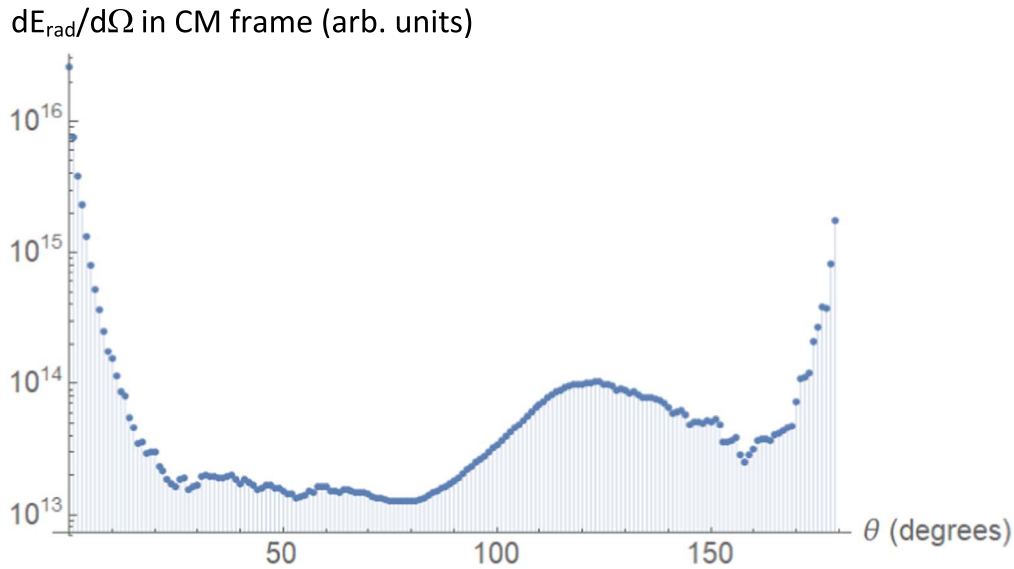


Figure 9. Global radiation angular distribution per unit solid angle in the center of the momentum frame, emitted by the spine electrons of the cylindrical shear boundary of Figure 8. Here θ is measured from the jet axis (x -axis) of Figure 8. The broad bump between 100° and 150° is contributed by high-energy spine electrons crossing the shear interface at large angles in the CM frame. A similar figure holds for the sheath electrons, but with the left and right reversed.

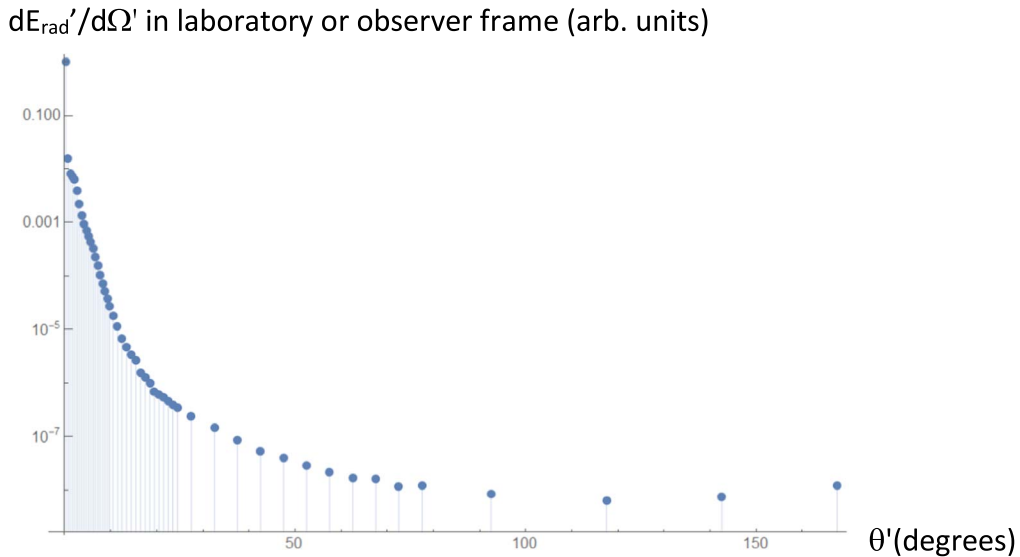


Figure 10. Global radiation angular distribution $dE'_{\text{rad}}/d\Omega'$ in the laboratory frame (LF = rest frame of the central engine or observer) emitted by the cylindrical shear boundary of Figure 8, as a function of observer view angle θ' from the jet axis in the LF. This radiation angular pattern is obtained by combining Figure 9 for the spine electrons with a similar plot from the sheath electrons, and then Lorentz boosting the total result to the LF. It shows a steep decrease with increasing θ' which moderates at larger angles. The small “kinks” at $\theta' \sim 2^\circ\text{--}5^\circ$ originate from Lorentz boosting the broad bump of Figure 9 at $100^\circ\text{--}150^\circ$ and a similar bump at $30^\circ\text{--}80^\circ$ from the sheath electrons. It is a tell-tale signature of relativistic SBL emission caused by electrons crossing the shear interface. The decrease of angular distribution with observer viewing angle is roughly consistent with the subluminal gamma-ray output of GW170817.

the current model based on a pure electron–ion plasma with no initial magnetic fields or e^+e^- pairs is a gross simplification of a realistic GRB jet. In Section 6 we will discuss the next steps in generalizing this model. GW170817/GRB 170817A (Abbott et al. 2017; LIGO et al 2017) was a highly subluminal short GRB (Berger 2014) from the merger of two neutron stars, whose jet axis is pointed at $>30^\circ$ from the observer (Figure 11; Mooley et al. 2018). If the jet body is narrow ($<5^\circ\text{--}10^\circ$) as in most GRBs, the observer would likely miss the front shock emission, which should be confined within a $5^\circ\text{--}10^\circ$ cone centered on the jet axis. In this case the observed prompt gamma rays may be dominated by the shear boundary emission along the side of the jet (Figure 11). In such a scenario, Figure 10 makes an important prediction: the

radiation observed at $\sim 20^\circ\text{--}25^\circ$ from the jet boundary should be $\sim 10^{-5}\text{--}10^{-6}$ of the radiation observed near the forward direction, after we take into account the $\sim 5^\circ\text{--}10^\circ$ angle between the jet boundary and the jet axis (Figure 11). Compared to the brightest short GRBs ($E_{\text{iso}} \sim 10^{52}$ erg, Meszneros 2002; Piran 2005; Berger 2014), GRB 170817A ($E_{\text{iso}} \sim 5 \times 10^{46}$ erg) is indeed fainter by a factor of $\sim 5 \times 10^{-6}$, consistent with Figure 10. Of course there are many unknown factors that make such a quantitative comparison questionable (e.g., dynamic range of short GRB’s intrinsic energy, bulk Lorentz factor of GW170817, jet opening angle, etc). But at least our SBL model prediction of radiation angular distribution is consistent with the subluminal nature of GRB 170817A. This should encourage us to explore using

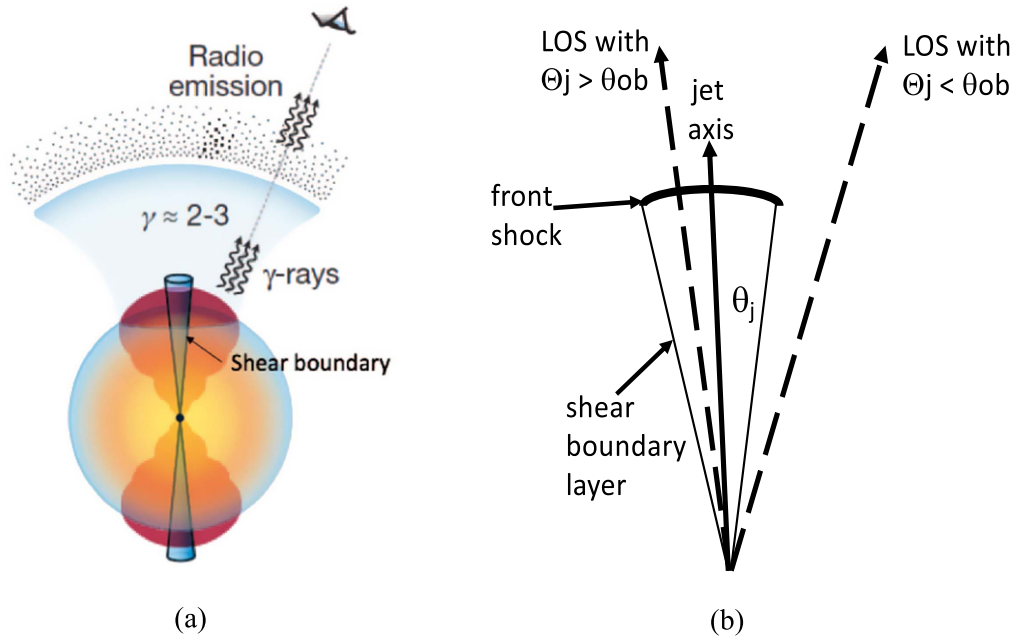


Figure 11. Artist sketch of the observer line of sight (LOS) vs. the jet axis for GW170817. Figure (a) is adapted from Mooley et al. (2018), showing the different emission regimes of a successful jet punching through the neutron star merger cloud or cocoon. Figure (b) illustrates the range of observer viewing angles at which shock emission dominates compared to the range of viewing angles at which shear boundary emission dominates. Since $\theta_{\text{ob}} > 30^\circ$ for GW170817, we expect the shear boundary emission to dominate if the intrinsic jet opening angle θ_j is $\ll 30^\circ$, which is expected for most GRB jets.

theoretical predictions such as Figure 10 to confront the statistics of the short GRB database (Berger 2014).

Despite the large viewing angle and highly subluminal gamma-ray output of GW170817, the observed spectral peak of its prompt gamma rays ($E_{\text{pk}} \sim 150$ keV, Abbott et al. 2017; Gill & Granot 2018) is only moderately below those of bright short GRBs, taking into account their redshifts (Berger 2014). However, to compare in detail the ω_{rad} predicted from our PIC simulation results with the observed spectral peak, we will need to carefully weigh the ω_{rad} values of Figure 6 with the number of photons emitted in each angular bin. Hence an accurate calculation of ω_{rad} as a function of observer viewing angle is extremely laborious and will be deferred to a future paper.

Dimensionally we can in principle constrain the magnetic field and baryon density using Equation (7): $\omega_{\text{rad}} \sim \gamma_c^2 \Omega_{\text{ce}}$ modulo a numerical factor of order unity, where Ω_{ce} is the electron gyrofrequency $eB/m_e c$. Using the energy partition of Figure 3, Liang et al. (2013) estimated the magnetic field B and plasma density n in the CM frame for typical GRBs with $E_{\text{pk}} \sim 250$ keV, $\Gamma \sim 450$, and showed that they are consistent with empirical observational constraints. If we assume similar Γ values for GW170817, then the (B, n) values of Liang et al. (2013) can be scaled to GW170817. Detailed modeling of GRB 170817A spectral data based on our SBL results will be presented in a future paper, after we have obtained an accurate estimate of ω_{rad} as a function of the observer viewing angle.

6. Discussion and Conclusions

In this work, we have presented the radiation of a kinetic collisionless relativistic shear boundary layer. Using EM field data from a specific PIC simulation, we compute a large ensemble of test electron trajectories as well as their radiated power and peak radiation frequency. We find that the most highly radiative electrons undergo looping motions and then cross the shear interface at large angles from the direction of

the bulk flow. This behavior contradicts the simple theoretical models of jet emission. Most models assume that highly radiating electrons emit isotropically in the jet rest frame, yielding radiation beamed into a narrow cone of half angle $\sim 1/\Gamma$ in the observer frame. Our result suggests that the complex behavior of highly radiative electrons at SBLs needs to be taken into account in order to accurately predict the radiation angular pattern as a function of the view angle. This result has important implications for the interpretation of GRB data whenever the observer angle from the jet axis is much larger than the jet body opening angle, where SBL emission likely dominates over the front shock emission. Statistically, large view angles may be common among nearby GRBs discovered through their gravitational wave signals, such as GW170817.

In this paper we have focused only on the electron trajectories and radiation properties of an idealized shear boundary of a uniform pure electron–ion plasma with no initial magnetic fields. For short GRBs from neutron star mergers such as the event associated with GW170817, the outflow is likely baryon dominated. In this case a model based on pure electron–ion plasma may be justifiable. In general, a GRB jet will likely have mixed composition (e.g., mixture of $e+e-$ pairs and e -ion plasmas), nonzero initial magnetic fields and large density contrast with the CSM, among other things. These additional complications lie beyond the scope of this paper and are currently under investigation by our group. However, we can speculate on some of their potential qualitative effects on the SBL radiation output.

In Liang et al. (2013), we have already investigated the effects of adding $e+e-$ pairs to an electron–ion plasma. We found that in addition to the d.c. slab fields exhibited in Figure 2, large amplitude electromagnetic waves develop in a zone just outside the d.c. slab fields. These waves stochastically accelerate some of the electrons and positrons to form a power-law tail above the ion kinetic energy. However, such wave acceleration occurs in EM fields much weaker than the d.c. slab

fields. While the detailed electron trajectories for this case have not yet been studied, we expect that (a) the radiation emitted by stochastic wave acceleration will be weaker than the acceleration by d.c. fields reported here, and (b) the radiation emitted by stochastic wave acceleration will not be narrowly beamed along the shear interface. We therefore speculate that the addition of a small amount of e^+e^- pairs to an electron-ion plasma will not significantly alter the main results presented here, but this remains to be confirmed. On the other hand, if the jet is composed of pure e^+e^- plasma, the physics of the SBL will be completely different (see Liang et al. 2017). But a pure e^+e^- jet seems unlikely for a neutron star merger event.

The effects of preexisting magnetic fields on the SBL radiation output is currently under detailed study. It is intuitive that longitudinal (i.e., poloidal) magnetic fields aligned with the flow direction will likely suppress or reduce the EKKHI and ECCI, since such fields inhibit electrons from streaming across the shear interface. On the other hand, transverse (i.e., toroidal) magnetic fields will either deflect electrons toward or away from the shear interface, depending on the polarity. Hence in general the effects of preexisting magnetic fields will be very complicated, depending on their strength, orientation, and polarity. It is impossible to predict a priori their net effect on the radiation output. Of course, if the preexisting field is so strong that the electron gyroradii become smaller than the electron skin depth, the plasma effectively becomes a fluid, and MHD replaces kinetic theory. In that case, MHD simulations predict that most of the shear flow energy will be converted into MHD turbulence and eventually get thermalized (Zhang et al. 2009). Hence the radiation will be dominated by isotropic thermal radiation.

The effects of density jumps across the shear flow boundary are also being studied. In general, the SBL structure and d.c. fields will become asymmetric on the two sides of the shear boundary. However, most of the results of this paper should still apply as long as the electron radiation is dominated by its trajectory lying solely on one side of the shear boundary.

This work was supported by National Science Foundation grant AST1313129 and Department Of Energy grant DE-SC0016505. We thank Yingchao Lu for the use of his computer time allocation on Stampede2 and Professor Anthony Chan for valuable discussions. The authors acknowledge the Texas Advanced Computing Center (TACC) at The University of Texas in Austin for providing HPC resources that have contributed to the research results reported in this paper.

ORCID iDs

Markus Boettcher  <https://orcid.org/0000-0002-8434-5692>

References

- Abbott, B., Abbott, R., Abbott, T. D., et al. 2017, *ApJL*, **848**, L13
- Alves, E. P., Grismayer, T., Fonseca, R. A., et al. 2014, *NJPh*, **16**, 035007
- Alves, E. P., Grismayer, T., Martins, S. F., et al. 2012, *ApJL*, **746**, L14
- Berezhko, E. G. 1981, *JETPL*, **33**, 399
- Berger, E. 2014, *ARA&A*, **52**, 43
- Birdsall, C. K., & Langdon, A. B. 1991, *Plasma Physics via Computer Simulation* (Bristol: IOP)
- Boettcher, M. 2007, *Ap&SS*, **309**, 95
- Boyd, T., & Sanderson, J. 2003, *Physics of Plasmas* (Cambridge: Cambridge Univ. Press)
- Brady, C., Bennett, K., Schimtz, H., & Ridgers, C. 2012, *EPOCH Users Manual v4.3.4* (Coventry: Univ. Warwick)
- Ghisellini, G., Tavecchio, F., Chiaberge, M., et al. 2005, *A&A*, **432**, 401
- Ghisellini, G., Tavecchio, F., Foschini, L., et al. 2010, *MNRAS*, **402**, 497
- Gill, T., & Granot, J. 2018, *MNRAS*, **478**, 4128
- Grismayer, T., Alves, E. P., Fonseca, R. A., & Silva, L. O. 2013, *PhRvL*, **111**, 015005
- Gruzinov, A. 2008, arXiv:0803.1182
- Hededal, C. 2005, PhD thesis, Niels Bohr Inst. (arXiv:astroph0506559)
- Hededal, C., & Norlund, A. 2005, arXiv:astroph0511662
- Kargaltsev, O., Cerutti, B., Lyubarsky, Y., & Striani, E. 2015, *SSRv*, **191**, 391
- Krall, & Trivelpiece 1973, *Principles of Plasma Physics* (New York: McGraw Hill)
- Landau, L. D., & Lifshitz, E. M. 1962, *The Classical Theory of Fields* (New York: Addison-Wesley)
- Langdon, A. B., & Lasinski, B. 1976, *MComP*, **16**, 327
- Liang, E., Fu, W., Boettcher, M., Smith, I., & Roustazadeh, P. 2013, *ApJL*, **779**, L27
- Liang, E., Fu, W., & Böttcher, M. 2017, *ApJ*, **847**, 90
- Liang, E., Fu, W., Böttcher, M., & Roustazadeh, P. 2018, *ApJ*, **854**, 129
- Liang, E., Wang, J., Lu, Y., & Zheng, K. 2020, *ApJ*, submitted
- LIGO, Abbott, R., Abbott, T. D., et al. 2017, *ApJL*, **848**, L12
- MacFadyen, A., & Woosley, S. E. 1999, *ApJ*, **524**, 262
- Meszeros, P. 2002, *ARA&A*, **40**, 137
- Mooley, K. P., Nakar, E., Hotokezaka, K., et al. 2018, *Natur*, **554**, 207
- Nishikawa, K.-I., Hardee, P., Minzuno, Y., et al. 2013, in *EPJ Web of Conf.* **61**, The Innermost Regions of Relativistic Jets and Their Magnetic Fields, ed. J. L. Gómez (Les Ulis: EDP Sciences), 02003
- Nishikawa, K., Frederiksen, J. T., Nordlund, Å., et al. 2016, *ApJ*, **820**, 94
- Nishikawa, K., Hardee, P. E., Duñan, I., et al. 2014, *ApJ*, **793**, 60
- Piran, T. 2005, *RvMP*, **76**, 1143
- Rieger, F., & Duffy, P. 2006, *ApJ*, **652**, 1044
- Rybicki, G., & Lightman, A. 1979, *Radiative Processes in Astrophysics* (New York: Wiley)
- Sironi, L., & Spitkovsky, A. 2009, *ApJL*, **707**, L92
- Stawarz, L., & Ostrowski, M. 2002, *ApJ*, **578**, 763
- Zhang, W., MacFadyen, A., & MacFadyen, P. 2009, *ApJL*, **692**, L40